

# Generalized Scattering Matrix Framework for Modeling Implantable Antennas in Multilayered Spherical Media

Chenbo Shi, Xin Gu, Shichen Liang and Jin Pan

**Abstract**—This paper presents a unified and efficient framework for analyzing antennas embedded in spherically stratified media—a model broadly applicable to implantable antennas in biomedical systems and radome-enclosed antennas in engineering applications. The proposed method decouples the modeling of the antenna and its surrounding medium by combining the antenna’s free-space generalized scattering matrix (GSM) with a set of extended spherical scattering operators (SSOs) that rigorously capture the electromagnetic interactions with multilayered spherical environments. This decoupling enables rapid reevaluation under arbitrary material variations without re-simulating the antenna, offering substantial computational advantages over traditional dyadic Green’s function (DGF)-based MoM approaches. The framework supports a wide range of spherical media, including radially inhomogeneous and uniaxially anisotropic layers. Extensive case studies demonstrate excellent agreement with full-wave and DGF-based solutions, confirming the method’s accuracy, generality, and scalability. Code implementations are provided to facilitate adoption and future development.

**Index Terms**—Generalized scattering matrix, implantable antennas, spherical layers, dyadic Green’s functions.

## I. INTRODUCTION

**I**MPLANTABLE antennas have received increasing attention in recent years due to their critical role in enabling in-body wireless communication, health monitoring, and telemedicine. In many studies, the electromagnetic environment surrounding an implantable antenna—such as human tissue—has been effectively modeled as a spherically stratified medium enclosing the antenna [1]–[6]. These layers often exhibit spatial inhomogeneity, anisotropy, and material loss. Beyond biomedical contexts, such spherical-layer models are also widely employed in engineering electromagnetics to characterize antennas enclosed by radomes, including those using metamaterial or metasurface shells engineered to exhibit tailored anisotropic properties. Consequently, the term “implantable antenna” used throughout this work is meant to broadly encompass both biological and engineered spherical encapsulation scenarios.

Direct numerical simulation of antennas embedded in spherical stratified media using commercial software is typically labor-intensive. A more practical approach combines closed-form dyadic Green’s functions (DGFs) for spherical layered

media [7]–[11] with the method of moments (MoM), thus avoiding full discretization of the spherical structure. While this hybrid approach improves computational efficiency compared to brute-force simulations, it still suffers from a major drawback: the MoM impedance matrix of the antenna is intrinsically dependent on the Green’s function, which itself varies with the material properties of the surrounding layers. Consequently, any modification to the spherical medium requires re-evaluation of the antenna system, severely limiting the method’s applicability in parametric sweeps or design optimization. As a result, it is only practical for structurally simple antenna configurations.

To overcome these limitations, this paper proposes a decoupled modeling framework that combines the generalized scattering matrix (GSM) of the antenna [12] with a set of extended spherical scattering operators (SSOs). Within this framework, the antenna and the surrounding medium are treated independently: the antenna is characterized via its GSM, which may be obtained from any frequency-domain solver in free space [13], or even from experimental measurement [14]; meanwhile, the influence of the spherical stratified environment is fully encapsulated by the SSOs. A key advantage of this decoupling is that once the antenna’s GSM is known, modifications to the spherical shell require only a recalculation of the SSOs—no further simulation of the antenna is needed. This dramatically reduces computational overhead and makes the method highly suitable for forward design and optimization of spherical-layered systems, such as radomes and dielectric cloaks [15].

Furthermore, the proposed framework accommodates a broad class of spherical environments, including arbitrarily layered media, radially varying uniaxial anisotropic materials, and even continuously inhomogeneous profiles. In most practical cases, the SSOs admit closed-form analytical expressions. When such expressions are unavailable, the governing differential equations are solved using robust numerical tools such as MATLAB’s ODE45, ensuring both generality and numerical stability. All source codes and computational routines are openly provided to facilitate reproducibility and adaptation to other application domains [16].

To rigorously validate the proposed approach, a series of case studies are presented, covering all major categories of spherical media mentioned above. The impact of the spherical shell on the antenna’s input matching, radiation characteristics, and bistatic radar cross section (RCS) is thoroughly examined. Excellent agreement is observed between our results, full-wave simulations (*e.g.*, using commercial software, FEKO),

Manuscript received Jul. 17, 2025. (Corresponding author: Jin Pan.)

Chenbo Shi, Xin Gu, Shichen Liang and Jin Pan are with the School of Electronic Science and Engineering, University of Electronic Science and Technology of China, Chengdu 611731 China (e-mail: chenbo\_shi@163.com; xin\_gu04@163.com; lscstu001@163.com; panjin@uestc.edu.cn).

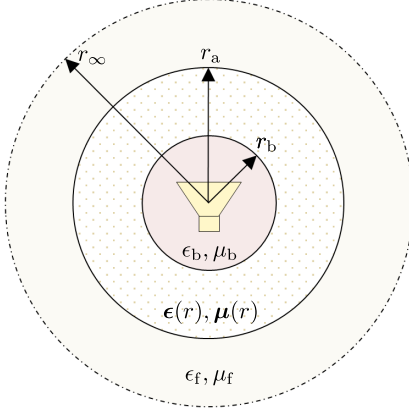


Fig. 1. Canonical model for an embedded or implantable antenna. The antenna is enclosed within a spherical bubble of radius  $r_b$  and constitutive parameters  $\epsilon_b$  and  $\mu_b$ . This bubble is surrounded by a spherical shell of outer radius  $r_a$ , whose material may be radially inhomogeneous and uniaxially anisotropic, described by spatially varying tensors  $\epsilon(r)$  and  $\mu(r)$ . The exterior region is homogeneous free space, characterized by  $\epsilon_f$  and  $\mu_f$ , typically taken as 1.

and problem-specific Green's function methods, while the proposed framework consistently achieves significantly greater computational efficiency.

## II. SPHERICAL WAVE DECOMPOSITION AND SCATTERING OPERATORS

Figure 1 depicts the canonical configuration considered in this work: an antenna is enclosed within a spherical encapsulation (bubble) of radius  $r_b$ , which is itself embedded in a multilayer spherical shell with outer radius  $r_a$ , potentially exhibiting radial inhomogeneity and anisotropy. The outermost region is free space. The shell is characterized by position-dependent constitutive tensors  $\epsilon(r)$  and  $\mu(r)$ , while both the inner bubble and free space are assumed homogeneous and isotropic.

In the isotropic regions, electromagnetic fields are expanded in terms of vector spherical wave functions (VSWFs) as

$$\begin{aligned} \mathbf{E}(\mathbf{r}) &= k\sqrt{Z} \sum_n a_n \mathbf{u}_n^{(1)}(k\mathbf{r}) + f_n \mathbf{u}_n^{(4)}(k\mathbf{r}) \\ \mathbf{H}(\mathbf{r}) &= \frac{jk}{\sqrt{Z}} \sum_n a_n \mathbf{u}_n^{(1)}(k\mathbf{r}) + f_n \mathbf{u}_n^{(4)}(k\mathbf{r}) \end{aligned} \quad (1)$$

where  $k$  and  $Z$  are the wavenumber and wave impedance of the corresponding medium (e.g.,  $k_b, Z_b$  in the bubble,  $k_f, Z_f$  in free space). The VSWFs  $\mathbf{u}_n^{(p)}$  are defined in Appendix A, with superscripts  $p = 1$  and  $p = 4$  denoting regular and outgoing waves, respectively. The multi-index  $n \rightarrow \tau\sigma ml$  includes polarization type  $\tau = \{1, 2\}$  (TE, TM), parity  $\sigma = \{e, o\}$ , degree  $l = \{1, 2, \dots, L_{\max}\}$ , and order  $m = \{0, 1, \dots, l\}$ . The truncation degree  $L_{\max}$  is estimated via [17]:

$$L_{\max} = \lceil k_f r_a + 7\sqrt[3]{k_f r_a} + 3 \rceil$$

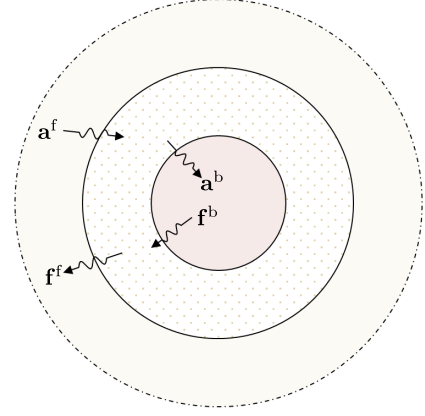


Fig. 2. Schematic of wave propagation and interaction in the layered spherical system. Regular waves incident from free space ( $\mathbf{a}^f$ ) are partially reflected and partially transmitted into the inner bubble. Conversely, outgoing waves radiated from the antenna inside the bubble ( $\mathbf{f}^b$ ) undergo partial transmission and reflection at the spherical shell.

Within the intermediate shell, fields admit a generalized expansion:

$$\begin{aligned} \mathbf{E}(\mathbf{r}) &= \sum_n \alpha_n \mathbf{w}_n(\mathbf{r}) \\ \mathbf{H}(\mathbf{r}) &= \frac{j}{k_0 Z_0} \sum_n \alpha_n \boldsymbol{\mu}^{-1}(\mathbf{r}) \cdot (\nabla \times \mathbf{w}_n(\mathbf{r})). \end{aligned} \quad (2)$$

Assuming radial uniaxial anisotropy, the constitutive tensors take the form:

$$\begin{aligned} \epsilon(r) &= \epsilon_{\perp}(r) (\mathbf{1}_3 - \hat{\mathbf{r}}\hat{\mathbf{r}}) + \epsilon_r(r) \hat{\mathbf{r}}\hat{\mathbf{r}} \\ \mu(r) &= \mu_{\perp}(r) (\mathbf{1}_3 - \hat{\mathbf{r}}\hat{\mathbf{r}}) + \mu_r(r) \hat{\mathbf{r}}\hat{\mathbf{r}}. \end{aligned} \quad (3)$$

where  $\mathbf{1}_3$  denotes the 3D identity dyadic. The basis functions  $\mathbf{w}_n(\mathbf{r})$  are constructed as [18, Ch. 8.4]:

$$\begin{aligned} \mathbf{w}_{1n} &= \frac{g(r)}{k_0 r} \mathbf{A}_{1n}(\hat{\mathbf{r}}) \\ \mathbf{w}_{2n} &= \frac{h'(r)}{k_0^2 r \epsilon_{\perp}(r)} \mathbf{A}_{2n}(\hat{\mathbf{r}}) + \frac{h(r) \sqrt{l(l+1)}}{k_0^2 \epsilon_r(r) r^2} \mathbf{A}_{3n}(\hat{\mathbf{r}}) \end{aligned} \quad (4)$$

where  $\mathbf{A}_{\tau n}(\mathbf{r})$  are vector spherical harmonics (see Appendix A). The radial functions  $g(r)$  and  $h(r)$  satisfy:

$$\begin{cases} g''(r) + p_1(r) g'(r) + q_1(r) g(r) = 0 \\ h''(r) + p_2(r) h'(r) + q_2(r) h(r) = 0 \end{cases} \quad (5)$$

with

$$\begin{aligned} p_1 &= -\frac{\mu'_{\perp}(r)}{\mu_{\perp}(r)}, q_1 = k_0^2 \mu_{\perp}(r) \epsilon_{\perp}(r) - \frac{\mu_{\perp}(r) l(l+1)}{\mu_r(r) r^2} \\ p_2 &= -\frac{\epsilon'_{\perp}(r)}{\epsilon_{\perp}(r)}, q_2 = k_0^2 \mu_{\perp}(r) \epsilon_{\perp}(r) - \frac{\epsilon_{\perp}(r) l(l+1)}{\epsilon_r(r) r^2}. \end{aligned} \quad (6)$$

Figure 2 illustrates the wave interactions in the layered shell. An incident regular wave  $\mathbf{a}^f$  from free space is partially scattered and partially transmitted into the bubble. Conversely, outgoing waves  $\mathbf{f}^b$  radiated from the antenna undergo partial reflection and transmission at the shell interface. These bidirectional interactions are captured by the SSO [19, Ch 3.5], [20], [21]:

$$\begin{bmatrix} \mathbf{f}^f \\ \mathbf{a}^b \end{bmatrix} = \begin{bmatrix} \mathbf{t} & \boldsymbol{\Psi} \\ \boldsymbol{\Phi} & \boldsymbol{\rho} \end{bmatrix} \begin{bmatrix} \mathbf{a}^f \\ \mathbf{f}^b \end{bmatrix} \quad (7)$$

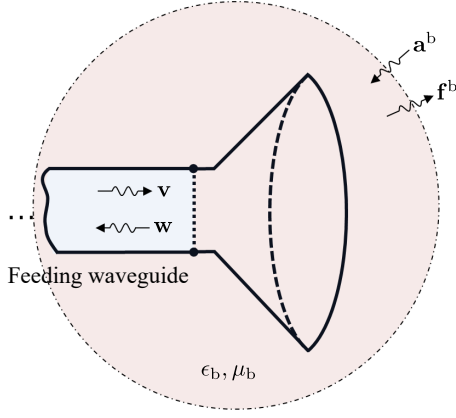


Fig. 3. Antenna in a bubble-material filled free space. Regular incident and outgoing spherical waves in the bubble are  $\mathbf{a}^b$  and  $\mathbf{f}^b$ , respectively. The antenna is interfaced with a waveguide supporting inward and outward modal amplitudes  $\mathbf{v}$  and  $\mathbf{w}$ .

Here,  $\mathbf{t}$  denotes the free-space transition matrix (T-matrix),  $\Phi$  and  $\Psi$  describe inward and outward transmission through the shell, and  $\rho$  accounts for internal reflection. In the absence of radiated waves from the antenna, *i.e.*,  $\mathbf{f}^b = \mathbf{0}$ , this relation reduces to the classical T-matrix scattering form:  $\mathbf{f}^f = \mathbf{t}\mathbf{a}^f$  [18], [22].

The antenna inside the bubble is excited by two types of inputs: waveguide modes  $\mathbf{v}$  and regular spherical waves  $\mathbf{a}^b$ , as illustrated in Fig. 3. In response, it produces reflected waveguide modes  $\mathbf{w}$  and radiated (and scattered) outgoing spherical waves  $\mathbf{f}^b$ . This interaction is governed by the GSM of the antenna (the source-scattering formulation [14, Ch. 2.3.5]):

$$\begin{bmatrix} \mathbf{w} \\ \mathbf{f}^b \end{bmatrix} = \begin{bmatrix} \mathbf{\Gamma} & \frac{1}{2}\mathbf{R} \\ \mathbf{T} & \frac{1}{2}(\tilde{\mathbf{S}} - \mathbf{1}) \end{bmatrix} \begin{bmatrix} \mathbf{v} \\ \mathbf{a}^b \end{bmatrix}. \quad (8)$$

Here,  $\mathbf{\Gamma}$  denotes the waveguide port S-parameters,  $\mathbf{R}$  and  $\mathbf{T}$  describe reception and transmission between the antenna and the spherical waves, and  $\mathbf{S}$  is the antenna's scattering matrix. All matrices are evaluated in an unbounded medium (free space) filled with the same material as the bubble.

Rewriting (8) explicitly as

$$\begin{cases} \mathbf{\Gamma}\mathbf{v} + \frac{1}{2}\mathbf{R}\mathbf{a}^b = \mathbf{w} \\ \mathbf{T}\mathbf{v} + \frac{1}{2}(\mathbf{S} - \mathbf{1})\mathbf{a}^b = \mathbf{f}^b \end{cases} \quad (9)$$

and substituting  $\mathbf{a}^b$  from (7) yields

$$\begin{cases} \mathbf{\Gamma}\mathbf{v} + \frac{1}{2}\mathbf{R}(\Phi\mathbf{a}^f + \rho\mathbf{f}^b) = \mathbf{w} \\ \mathbf{T}\mathbf{v} + \frac{1}{2}(\mathbf{S} - \mathbf{1})(\Phi\mathbf{a}^f + \rho\mathbf{f}^b) = \mathbf{f}^b. \end{cases} \quad (10)$$

Solving the second equation for  $\mathbf{f}^b$  gives:

$$\mathbf{f}^b = \mathbf{M}^{-1} \left[ \mathbf{T}\mathbf{v} + \frac{1}{2}(\mathbf{S} - \mathbf{1})\Phi\mathbf{a}^f \right] \quad (11)$$

where  $\mathbf{M} = [\mathbf{1} - \frac{1}{2}(\mathbf{S} - \mathbf{1})\rho]$ . Substituting this result into the expression for  $\mathbf{w}$  leads to:

$$\begin{aligned} & \left[ \mathbf{\Gamma} + \frac{1}{2}\mathbf{R}\rho\mathbf{M}^{-1}\mathbf{T} \right] \mathbf{v} \\ & + \frac{1}{2}\mathbf{R} \left[ \Phi + \rho\mathbf{M}^{-1}\frac{1}{2}(\mathbf{S} - \mathbf{1})\Phi \right] \mathbf{a}^f = \mathbf{w}. \end{aligned} \quad (12)$$

From (7), we have  $\mathbf{f}^f = \mathbf{t}\mathbf{a}^f + \Psi\mathbf{f}^b$ , which, inserting (11), becomes

$$\mathbf{f}^f = \Psi\mathbf{M}^{-1}\mathbf{T}\mathbf{v} + \left[ \mathbf{t} + \Psi\mathbf{M}^{-1}\frac{1}{2}(\mathbf{S} - \mathbf{1})\Phi \right] \mathbf{a}^f. \quad (13)$$

By defining the effective scattering matrices as

$$\begin{aligned} \tilde{\mathbf{\Gamma}} &= \mathbf{\Gamma} + \frac{1}{2}\mathbf{R}\rho\mathbf{M}^{-1}\mathbf{T} \\ \tilde{\mathbf{R}} &= \mathbf{R} \left[ \Phi + \rho\mathbf{M}^{-1}\frac{1}{2}(\mathbf{S} - \mathbf{1})\Phi \right] \\ \tilde{\mathbf{T}} &= \Psi\mathbf{M}^{-1}\mathbf{T} \\ \tilde{\mathbf{S}} &= \mathbf{1} + 2\mathbf{t} + \Psi\mathbf{M}^{-1}(\mathbf{S} - \mathbf{1})\Phi. \end{aligned} \quad (14)$$

we obtain the final effective scattering formulation:

$$\begin{bmatrix} \mathbf{w} \\ \mathbf{f}^f \end{bmatrix} = \begin{bmatrix} \tilde{\mathbf{\Gamma}} & \frac{1}{2}\tilde{\mathbf{R}} \\ \tilde{\mathbf{T}} & \frac{1}{2}(\tilde{\mathbf{S}} - \mathbf{1}) \end{bmatrix} \begin{bmatrix} \mathbf{v} \\ \mathbf{a}^f \end{bmatrix}. \quad (15)$$

In practical settings, the excitations  $\mathbf{v}$  and  $\mathbf{a}^f$  are known, while the observable quantities  $\mathbf{w}$  and  $\mathbf{f}^f$  are directly computed from Eq.(15). The effective matrices  $\tilde{\mathbf{\Gamma}}$ ,  $\tilde{\mathbf{R}}$ ,  $\tilde{\mathbf{T}}$ , and  $\tilde{\mathbf{S}}$  preserve the physical interpretations of their counterparts in Eq.(8), now incorporating the full electromagnetic response of the spherical environment shown in Fig. 1.

### III. DETERMINATION OF THE SCATTERING OPERATORS

To evaluate the effective scattering parameters  $\tilde{\mathbf{\Gamma}}$ ,  $\tilde{\mathbf{R}}$ ,  $\tilde{\mathbf{T}}$ ,  $\tilde{\mathbf{S}}$ , one must compute both the GSM of the standalone antenna, *i.e.*,  $\mathbf{\Gamma}$ ,  $\mathbf{R}$ ,  $\mathbf{T}$ ,  $\mathbf{S}$ , and the SSOs  $\mathbf{t}$ ,  $\Phi$ ,  $\Psi$ ,  $\rho$ . These components are mutually independent and can therefore be determined separately.

#### A. Generalized Scattering Matrix of the Antenna

The submatrices  $\mathbf{\Gamma}$ ,  $\mathbf{R}$ ,  $\mathbf{T}$ ,  $\mathbf{S}$  characterize the antenna in an unbounded medium with identical material properties to those of the bubble. These parameters can be obtained numerically via full-wave methods such as the MoM or finite element analysis (FEA) [23], [24]. If the bubble medium is air or vacuum, these matrices may also be measured experimentally using spherical near-field measurement techniques. In this work, we employ a MoM-based simulation strategy [24].

#### B. Spherical Scattering Operators

1) *t matrix and  $\Phi$  matrix*: To compute the transition matrix  $\mathbf{t}$ , we consider the scenario where the bubble contains no internal source, *i.e.*,  $\mathbf{f}^b = \mathbf{0}$ . In this case, (7) simplifies to  $\mathbf{f}^f = \mathbf{t}\mathbf{a}^f$  and  $\mathbf{a}^b = \Phi\mathbf{a}^f$ .

At the innermost interface  $r = r_b$ , continuity of the tangential electromagnetic fields and orthogonality of the vector spherical harmonics  $\mathbf{A}_{\tau n}$  yield the following boundary conditions for TE ( $\tau = 1$ ) and TM ( $\tau = 2$ ) modes (some algebraic identities may be found in [18, Ch. 8.4]), respectively:

$$\begin{aligned} k_b \sqrt{Z_b} a_{1n}^b R_{1l}^{(1)}(k_b r_b) &= \alpha_{1n} \frac{g(r_b)}{k_0 r_b} \\ \frac{k_b}{\sqrt{Z_b}} a_{1n}^b R_{2l}^{(1)}(k_b r_b) &= \alpha_{1n} \frac{1}{Z_0} \frac{g'(r_b)}{\mu_{\perp}(r_b) k_0^2 r_b} \end{aligned} \quad (16)$$

for TE modes, and

$$\begin{aligned} k_b \sqrt{Z_b} a_{2n}^b R_{2l}^{(1)}(k_b r_b) &= \alpha_{2n} \frac{h'(r_b)}{k_0^2 r_b \epsilon_{\perp}(r_b)} \\ \frac{k_b}{\sqrt{Z_b}} a_{2n}^b R_{1l}^{(1)}(k_b r_b) &= \alpha_{2n} \frac{1}{Z_0} \frac{h(r_b)}{k_0 r_b} \end{aligned} \quad (17)$$

for TM modes.

From the above, the initial conditions for  $g(r)$  and  $h(r)$  are derived as:

$$\begin{aligned} \frac{g'(r_b)}{g(r_b)} &= \frac{k_b \mu_{\perp}(r_b)}{\mu_b} \frac{\psi_l'(k_b r_b)}{\psi_l(k_b r_b)} \\ \frac{h'(r_b)}{h(r_b)} &= \frac{k_b \epsilon_{\perp}(r_b)}{\epsilon_b} \frac{\psi_l'(k_b r_b)}{\psi_l(k_b r_b)}. \end{aligned} \quad (18)$$

with normalization  $g(r_b) = h(r_b) = 1$ . These are then used to solve the radial ordinary differential equations (ODEs) in (5). In this formulation, we also employ the standard algebraic relations connecting  $R_{\tau l}^{(p)}$  to the Riccati-Bessel functions  $\psi_l$  and  $\xi_l$ , as outlined in Appendix A.

At the outer interface  $r = r_a$ , applying field continuity again (noting  $f_{\tau n}^f = t_{\tau n} a_{\tau n}^f$ ), we obtain the following:

$$\begin{aligned} \alpha_{1n} \frac{g(r_a)}{k_0 r_a} &= k_f \sqrt{Z_f} a_{1n}^f \left[ R_{1l}^{(1)}(k_f r_a) + t_{1n} R_{1l}^{(4)}(k_f r_a) \right] \\ \alpha_{1n} \frac{1}{Z_0} \frac{g'(r_a)}{\mu_{\perp}(r_a) k_0^2 r_a} &= \frac{k_f a_{1n}^f}{\sqrt{Z_f}} \left[ R_{2l}^{(1)}(k_f r_a) + t_{1n} R_{2l}^{(4)}(k_f r_a) \right] \end{aligned} \quad (19)$$

and

$$\begin{aligned} \alpha_{2n} \frac{h'(r_a)}{k_0^2 r_a \epsilon_{\perp}(r_a)} &= k_f \sqrt{Z_f} a_{2n}^f \left[ R_{2l}^{(1)}(k_f r_a) + t_{2n} R_{2l}^{(4)}(k_f r_a) \right] \\ \alpha_{2n} \frac{1}{Z_0} \frac{h(r_a)}{k_0 r_a} &= \frac{k_f a_{2n}^f}{\sqrt{Z_f}} \left[ R_{1l}^{(1)}(k_f r_a) + t_{2n} R_{1l}^{(4)}(k_f r_a) \right]. \end{aligned} \quad (20)$$

Solving the above boundary-matching equations yields explicit closed-form expressions for the entries of the transition matrix  $\mathbf{t}$ , namely:

$$\begin{aligned} t_{1n} &= - \frac{\frac{\mu_f}{k_f \mu_{\perp}(r_a)} \frac{g'(r_a)}{g(r_a)} \psi_l(k_f r_a) - \psi_l'(k_f r_a)}{\frac{\mu_f}{k_f \mu_{\perp}(r_a)} \frac{g'(r_a)}{g(r_a)} \xi_l(k_f r_a) - \xi_l'(k_f r_a)} \\ t_{2n} &= - \frac{\frac{\epsilon_f}{k_f \epsilon_{\perp}(r_a)} \frac{h'(r_a)}{h(r_a)} \psi_l(k_f r_a) - \psi_l'(k_f r_a)}{\frac{\epsilon_f}{k_f \epsilon_{\perp}(r_a)} \frac{h'(r_a)}{h(r_a)} \xi_l(k_f r_a) - \xi_l'(k_f r_a)} \end{aligned} \quad (21)$$

The corresponding entries of the inward transmission matrix  $\Phi$  can be obtained by eliminating the coefficients  $\alpha_{\tau n}$  from the continuity relations, e.g., (16), (19) and (17), (20), yielding:

$$\begin{aligned} \Phi_{1n} &= \frac{a_{1n}^b}{a_{1n}^f} = \frac{g(r_b)}{g(r_a)} \frac{\sqrt{Z_f}}{\sqrt{Z_b}} \frac{\psi_l(k_f r_a) + t_{1n} \xi_l(k_f r_a)}{\psi_l(k_b r_b)} \\ \Phi_{2n} &= \frac{a_{2n}^b}{a_{2n}^f} = \frac{h'(r_b)}{h'(r_a)} \frac{\epsilon_{\perp}(r_a)}{\epsilon_{\perp}(r_b)} \frac{\sqrt{Z_f}}{\sqrt{Z_b}} \frac{\psi_l'(k_f r_a) + t_{2n} \xi_l'(k_f r_a)}{\psi_l'(k_b r_b)} \end{aligned} \quad (22)$$

As evident from (21) and (22), both  $\mathbf{t}$  and  $\Phi$  are diagonal matrices with entries dependent solely on the modal indices  $(\tau, l)$ .

2)  $\rho$  matrix and  $\Psi$  matrix: The derivation of the reflection matrix  $\rho$  and the outward transmission matrix  $\Psi$  proceeds analogously, now assuming no excitation from outside, i.e.,  $\mathbf{a}^f = \mathbf{0}$ . In this case, the relations simplify to  $\mathbf{a}^b = \rho \mathbf{f}^b$  and  $\mathbf{f}^f = \Psi \mathbf{f}^b$ . The corresponding initial conditions are set at the outer interface  $r = r_a$ :

$$\begin{aligned} \frac{g'(r_a)}{g(r_a)} &= \frac{k_f \mu_{\perp}(r_a)}{\mu_f} \frac{\xi_l'(k_f r_a)}{\xi_l(k_f r_a)} \\ \frac{h'(r_a)}{h(r_a)} &= \frac{k_f \epsilon_{\perp}(r_a)}{\epsilon_f} \frac{\xi_l'(k_f r_a)}{\xi_l(k_f r_a)}. \end{aligned} \quad (23)$$

These relations mirror those in (18), under the duality mapping:  $r_b \leftrightarrow r_a$ ,  $k_b \leftrightarrow k_f$ ,  $\mu_b \leftrightarrow \mu_f$ ,  $\epsilon_b \leftrightarrow \epsilon_f$ , and  $\psi_l \leftrightarrow \xi_l$ . Thus, one can directly write the closed-form expressions for  $\rho_{\tau n}$  and  $\Psi_{\tau n}$  as

$$\begin{aligned} \rho_{1n} &= - \frac{\frac{\mu_b}{k_b \mu_{\perp}(r_b)} \frac{g'(r_b)}{g(r_b)} \xi_l(k_b r_b) - \xi_l'(k_b r_b)}{\frac{\mu_b}{k_b \mu_{\perp}(r_b)} \frac{g'(r_b)}{g(r_b)} \psi_l(k_b r_b) - \psi_l'(k_b r_b)} \\ \rho_{2n} &= - \frac{\frac{\epsilon_b}{k_b \epsilon_{\perp}(r_b)} \frac{h'(r_b)}{h(r_b)} \xi_l(k_b r_b) - \xi_l'(k_b r_b)}{\frac{\epsilon_b}{k_b \epsilon_{\perp}(r_b)} \frac{h'(r_b)}{h(r_b)} \psi_l(k_b r_b) - \psi_l'(k_b r_b)} \end{aligned} \quad (24)$$

and ( $t_{\tau n} \leftrightarrow \rho_{\tau n}$  in (22))

$$\begin{aligned} \Psi_{1n} &= \frac{g(r_a)}{g(r_b)} \frac{\sqrt{Z_b}}{\sqrt{Z_f}} \frac{\rho_{1n} \psi_l(k_b r_b) + \xi_l(k_b r_b)}{\xi_l(k_f r_a)} \\ \Psi_{2n} &= \frac{h'(r_a)}{h'(r_b)} \frac{\epsilon_{\perp}(r_b)}{\epsilon_{\perp}(r_a)} \frac{\sqrt{Z_b}}{\sqrt{Z_f}} \frac{\rho_{2n} \psi_l'(k_b r_b) + \xi_l'(k_b r_b)}{\xi_l'(k_f r_a)} \end{aligned} \quad (25)$$

It is readily verified that  $\Phi = \Psi$  when the bubble medium is identical to the surrounding free space.

#### IV. NUMERICAL EXAMPLES

This section presents a series of representative examples to validate the accuracy, flexibility, and computational advantages of the proposed method. The structure under investigation is a multimode horn antenna, identical in geometry to that used in [24], situated inside a spherically layered medium in Fig. 1. The antenna is discretized using 5901 RWG basis functions [25] and supports five operating modes over the 3.2-3.8 GHz band: TE<sub>10</sub>, TE<sub>20</sub>, TE<sub>01</sub>, TE<sub>11</sub>, and TM<sub>11</sub>. Both the inner bubble and the outer free space are modeled as vacuum (or air), and all material variations are confined to the intermediate spherical shell.

##### A. Homogeneous Isotropic Medium

The first scenario considers a homogeneous, isotropic, lossy medium in the intermediate layer, with relative permittivity  $\epsilon_r = \epsilon_{\perp} = 5 - 0.5j$  and permeability  $\mu_r = \mu_{\perp} = 1$ . The inner and outer shell radii are  $r_b = 150$  mm and  $r_a = 180$  mm, respectively.

Under these conditions, the radial ODEs in (5) admit closed-form solutions:

$$\begin{aligned} g(r) &= A \psi_l(k_{\perp} r) + B \xi_l(k_{\perp} r) \\ h(r) &= C \psi_l(k_{\perp} r) + D \xi_l(k_{\perp} r) \end{aligned} \quad (26)$$



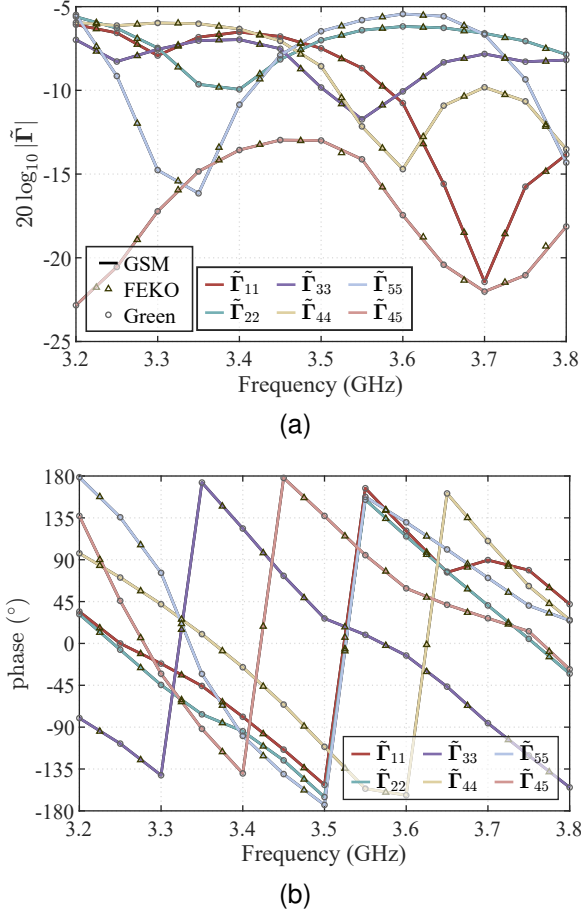


Fig. 4. Port S-parameters of a multimode horn antenna embedded in an isotropic and homogeneous spherical shell ( $\epsilon_r = \epsilon_\perp = 5 - 0.5j$ ,  $\mu_r = \mu_\perp = 1$ ). (a) Amplitude (in dB); (b) Phase (in degrees). Solid lines (labeled “GSM”) are computed using the proposed framework. Circles (labeled “Green”) are obtained from a method combining the problem-specific DGF with MoM. Modes 1 to 5 correspond to TE<sub>10</sub>, TE<sub>20</sub>, TE<sub>01</sub>, TE<sub>11</sub>, and TM<sub>11</sub>, respectively.

where  $k_\perp = k_0 \sqrt{\epsilon_\perp \mu_\perp}$ . The constants  $A, B, C, D$  are determined via boundary conditions from (18) or (23), yielding the scattering matrices  $\mathbf{t}, \Phi, \rho, \Psi$  through (21), (22) and (24), (25), respectively. The complete electromagnetic behavior is then computed using (15).

Figs. 4a and 4b show the amplitude and phase of the resulting port S-parameters. Results labeled “GSM” are obtained via our method and are in excellent agreement with full-wave simulations performed using FEKO.

To compute the radiation pattern under waveguide-mode excitation ( $\mathbf{a}^f = \mathbf{0}$ ), the outgoing spherical wave amplitudes are given by  $\mathbf{f}^f = \tilde{\mathbf{T}}\mathbf{v}$ , resulting in the far-field expression [20]:

$$\mathbf{F}(\hat{\mathbf{r}}) = \sqrt{Z_f} \sum_n f_{\tau n}^f j^{l+2-\tau} \mathbf{A}_{\tau n}(\hat{\mathbf{r}}). \quad (27)$$

Fig. 5 plots the gain patterns in the  $xoz$ -plane (for TE<sub>01</sub> mode, the E-plane) at 3.2 GHz for each waveguide mode. All results agree well with FEKO simulations.

Scattering analysis is performed by setting  $\mathbf{v} = \mathbf{0}$ , which leads to  $\mathbf{f}^f = \frac{1}{2}(\tilde{\mathbf{S}} - \mathbf{1})\mathbf{a}^f$ . The resulting bistatic RCS under plane-wave incidence from multiple angles is shown

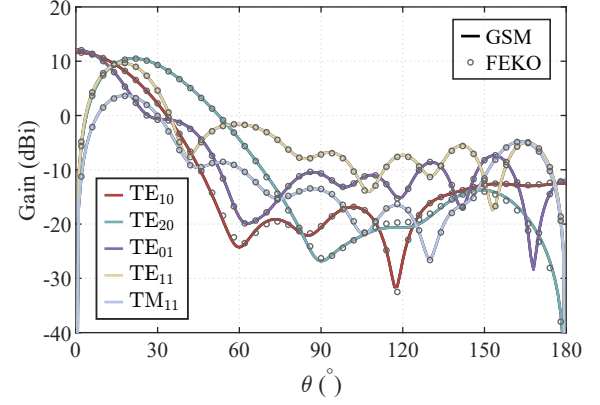


Fig. 5. Far-field gain patterns on the  $xoz$  plane at 3.2 GHz for the multimode horn antenna embedded in an isotropic homogeneous spherical shell. Each curve corresponds to a distinct waveguide excitation mode among TE<sub>10</sub>, TE<sub>20</sub>, TE<sub>01</sub>, TE<sub>11</sub>, and TM<sub>11</sub>.

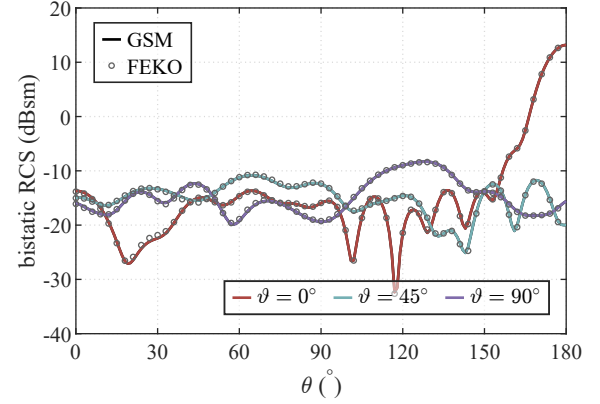


Fig. 6. Bistatic RCS on the  $xoz$  plane at 3.5 GHz for the multimode horn antenna embedded in an isotropic homogeneous spherical shell. Results are shown for three plane-wave incidence angles:  $\vartheta = 0^\circ, 45^\circ$ , and  $90^\circ$ .

in Fig. 6. Plane-wave excitation coefficients  $\mathbf{a}^f$  are computed using formulas from [24, Appendix A]. Results again match FEKO closely, with minor differences attributable to geometric discretization of the spherical shell.

The FEKO simulation uses 30,808 triangular elements with  $\lambda/10$  resolution, and relies on the multilevel fast multipole algorithm (MLFMA), yet remains computationally intensive. In contrast, our method requires only 0.3 seconds per evaluation after a one-time precomputation of the antenna’s free-space GSM (19 seconds).

For comparison, a problem-specific MoM implementation using a closed-form DGF tailored to this spherical geometry—labeled as “Green” in Fig. 4—achieves results identical to ours, with a runtime of 24.5 seconds. This significantly outperforms FEKO for a single evaluation but slightly lags behind our method in efficiency. Notably, in parametric studies where only the spherical shell’s material properties vary, our method reuses the precomputed GSM and remains at 0.3 seconds per case, while the “Green” method must regenerate the full solution, taking around 24.5 seconds.

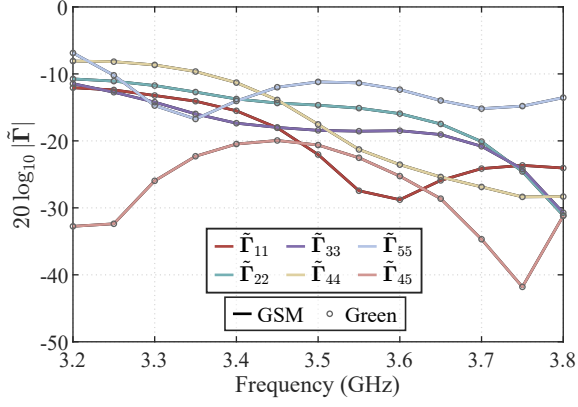


Fig. 7. Amplitude of port S-parameters for the multimode horn antenna embedded in a uniaxially anisotropic and homogeneous spherical shell ( $\epsilon_r = 2$ ,  $\epsilon_{\perp} = 5$ ,  $\mu_r = 1$ ,  $\mu_{\perp} = 3$ ).

### B. Homogeneous Anisotropic Medium

This case considers a homogeneous uniaxially anisotropic shell with  $\epsilon_r = 2$ ,  $\epsilon_{\perp} = 5$ ,  $\mu_r = 1$ , and  $\mu_{\perp} = 3$ . The shell geometry remains unchanged. Here, the solutions to (5) are:

$$\begin{aligned} g(r) &= A\psi_{L_1}(k_{\perp}r) + B\xi_{L_1}(k_{\perp}r) \\ h(r) &= C\psi_{L_2}(k_{\perp}r) + D\xi_{L_2}(k_{\perp}r) \end{aligned} \quad (28)$$

with modified angular indices:

$$\begin{aligned} L_1 &= \sqrt{\frac{\mu_{\perp}}{\mu_r}l(l+1) + \frac{1}{4}} - \frac{1}{2} \\ L_2 &= \sqrt{\frac{\epsilon_{\perp}}{\epsilon_r}l(l+1) + \frac{1}{4}} - \frac{1}{2}. \end{aligned} \quad (29)$$

The constants  $A, B, C, D$  are determined through (18) and (23).

Mainstream solvers such as FEKO, HFSS, or CST do not support radially anisotropic media. However, the associated dyadic Green's function is analytically tractable [26] and can be incorporated into a MoM solver. As shown in Fig. 7, the S-parameters computed using our framework closely match those from this specialized method. In addition, our formulation decouples the antenna and spherical layers, allowing material updates with minimal recomputation.

### C. Radially Piecewise Homogeneous Medium

We now consider a layered spherical shell consisting of multiple concentric regions, as illustrated in Fig. 8. Since  $\epsilon(r)$  and  $\mu(r)$  are discontinuous at the interfaces, the ODEs (5) are solved piecewise.

Let  $g_i(r)$  and  $h_i(r)$  be the solutions within the  $i$ -th layer, following the same form as (28), with layer-specific material parameters. Continuity of tangential fields across each interface at  $r = r_i$  imposes:

$$\begin{aligned} g_i(r_i) &= g_{i+1}(r_i), h_i(r_i) = h_{i+1}(r_i) \\ \frac{g'_i(r_i)}{\mu_{\perp i}(r_i)} &= \frac{g'_{i+1}(r_i)}{\mu_{\perp i+1}(r_i)}, \frac{h'_i(r_i)}{\epsilon_{\perp i}(r_i)} = \frac{h'_{i+1}(r_i)}{\epsilon_{\perp i+1}(r_i)}. \end{aligned} \quad (30)$$

This allows recursive evaluation from one layer to the next. As described in Sec. III-B, the matrices  $\mathbf{t}, \Phi$  are computed in

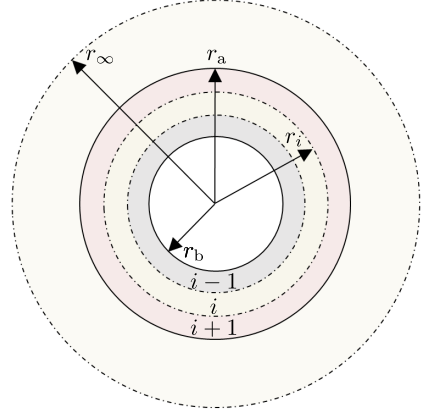


Fig. 8. Schematic of a spherically stratified structure consisting of multiple uniformly layered media. The  $i$ th interface at radius  $r = r_i$  separates region  $i$  and region  $i+1$ , with region indices increasing outward from the sphere center.

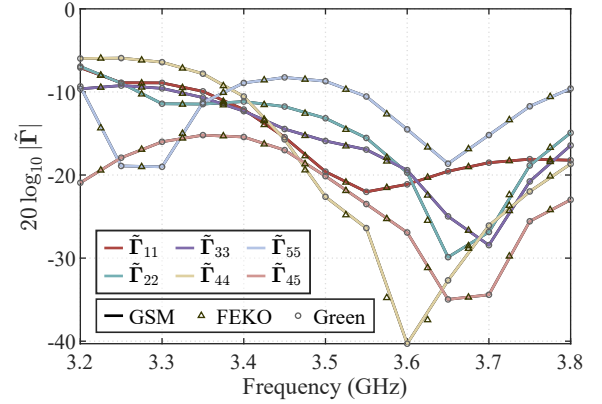


Fig. 9. Amplitude of port S-parameters for the multimode horn antenna embedded in a two-layer isotropic and homogeneous spherical shell ( $\epsilon_{r1} = \epsilon_{\perp 1} = 4.4 - 0.604j$ ,  $\epsilon_{r2} = \epsilon_{\perp 2} = 10$ ). Results from three different methods are compared.

the forward direction (inner to outer), while  $\rho, \Psi$  are obtained in reverse.

In the first example here, two 15-mm-thick isotropic layers are considered with parameters  $\epsilon_{r1} = \epsilon_{\perp 1} = 4.4 - 0.604j$  and  $\epsilon_{r2} = \epsilon_{\perp 2} = 10$ . Results from our method, the Green's function approach, and FEKO are shown in Figs. 9 and 10. The first two agree almost perfectly; deviations in FEKO stem from discretization on curved interfaces.

In the second example, the layers are uniaxially anisotropic:  $\epsilon_{r1} = 2$ ,  $\epsilon_{\perp 1} = 4.4$ ,  $\mu_{r1} = \mu_{\perp 1} = 2.2$ ; and  $\epsilon_{r2} = 1$ ,  $\epsilon_{\perp 2} = 8$ ,  $\mu_{r2} = 2$ ,  $\mu_{\perp 2} = 5$ . Fig. 11 confirms that our results remain highly accurate.

### D. Radially Piecewise Nonhomogeneous Medium

We now extend the framework to radially continuous but nonhomogeneous media, such as:

$$\begin{aligned} \epsilon_{\perp 1}(r) &= 5 \tan \frac{\pi}{5r}, \epsilon_{r1}(r) = 1 + \exp\left(2 \sin \frac{4}{r}\right) \\ \epsilon_{\perp 2}(r) &= 2 + \ln\left(\frac{2}{r} - 5\right), \epsilon_{r2}(r) = \frac{1}{r} \end{aligned}$$

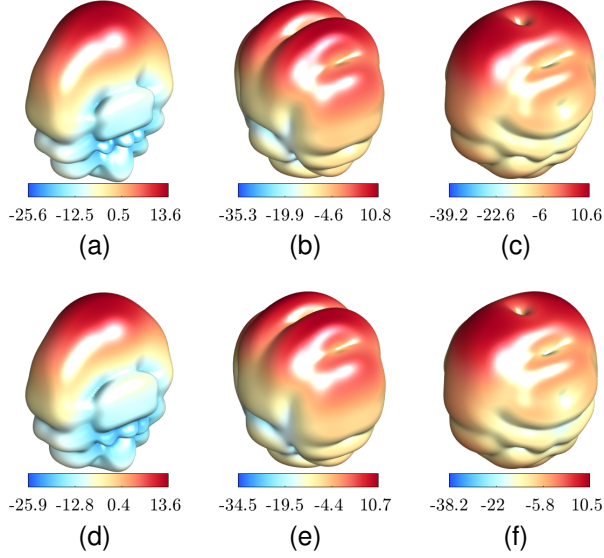


Fig. 10. Far-field gain patterns. The top panel shows results from full-wave simulations using FEKO, while the bottom panel shows results from the proposed method. (a), (d): TE<sub>10</sub> excitation; (b), (e): TE<sub>11</sub> excitation; (c), (f): TM<sub>11</sub> excitation.

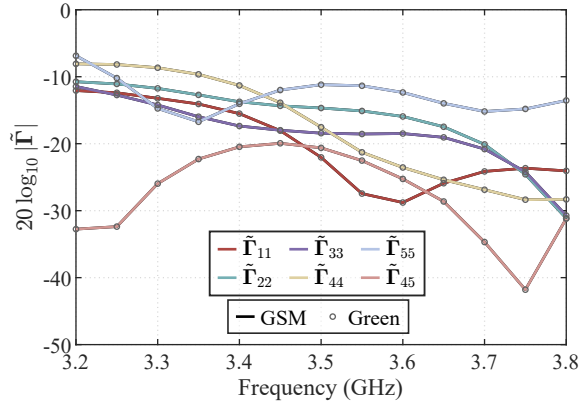


Fig. 11. Amplitude of port S-parameters for a multimode horn antenna embedded in a two-layer uniaxially anisotropic and homogeneous spherical shell ( $\epsilon_{r1} = 2, \epsilon_{\perp 1} = 4.4, \mu_{r1} = \mu_{\perp 1} = 2.2$  and  $\epsilon_{r2} = 1, \epsilon_{\perp 2} = 8, \mu_{r2} = 2, \mu_{\perp 2} = 5$ ).

with all permeabilities set to 1.

Since analytical solutions to (5) are unavailable, we employ MATLAB's `ode45` to numerically solve the radial equations. Code is provided to facilitate replication and customization [16].

To validate this result, the shell is approximated using 20 homogeneous anisotropic layers, whose parameters match the continuous profile at sampled radii. As shown in Fig. 12, the S-parameters obtained via the ODE solver and via the layered approximation agree remarkably well, confirming the robustness and flexibility of the proposed method.

## V. CONCLUSION AND DISCUSSION

This work introduces a unified framework for modeling antennas embedded in spherically stratified media, based on the combination of the antenna's GSM in free space and

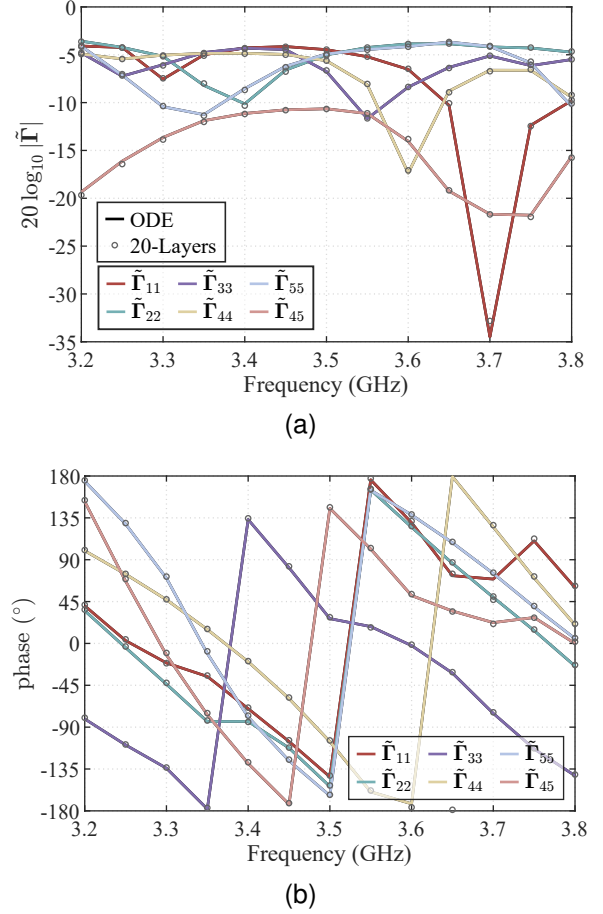


Fig. 12. Port S-parameters of the multimode horn antenna embedded in a two-layer radially continuous uniaxially anisotropic spherical shell. (a) Amplitude (in dB); (b) Phase (in degrees). The curve labeled “ODE” is obtained by directly solving the radial differential equations, (5). The circles labeled “20-Layers” corresponds to a 20-layer piecewise-uniform anisotropic approximation.

a set of analytically or numerically tractable SSOs. By decoupling the antenna from the surrounding electromagnetic environment, the proposed method enables rapid analysis of antenna behavior under arbitrary changes in the spherical medium—without requiring re-simulation of the antenna itself. Compared to conventional DGF-based methods or brute-force full-wave simulations, this approach significantly improves computational efficiency and flexibility, especially for parametric studies or design optimization.

A key strength of the proposed formulation is its wide applicability. It supports a broad range of spherical environments, including multilayered, radially inhomogeneous, and uniaxially anisotropic media. In cases where analytical solutions are not feasible, the required radial ODEs can be solved with standard numerical integrators (*e.g.*, MATLAB's `ode45`), without compromising generality or precision.

Another unique feature lies in the use of the antenna's GSM in free space—a quantity that can be obtained from numerical solvers or directly measured through calibrated multi-mode testing. This opens up new opportunities to incorporate realistic antenna characteristics such as manufacturing tolerances, connector mismatch, or near-field deformations, which are

difficult to capture using simulation models. Consequently, our method offers a practical means for statistically evaluating embedded antenna performance across a population of imperfect prototypes. If the antenna's GSM has been calibrated, the proposed framework can also quantify the deviation introduced by real-world fabrication of spherical shells from their idealized electromagnetic designs—making it valuable for assessing radome manufacturing tolerances.

Moreover, the approach extends naturally to array configurations. The GSM of an entire antenna array can be constructed from the GSMs of its individual elements [27] using spherical-wave translation theory. Therefore, the proposed method remains applicable to array antennas embedded in spherical environments: once the element-level GSM is known, system-level performance can be rapidly evaluated for various shell designs and material configurations.

It is worth noting that, at present, the formulation is limited to spherical shells composed of uniaxially anisotropic media. Extensions to handle general anisotropy, such as biaxial or non-symmetric tensor materials, remain a compelling direction for future work. However, this limitation pertains only to the expressibility of the SSOs, and does not affect the overall architecture or core methodology of the proposed framework.

In summary, this study presents a robust, efficient, and extensible modeling paradigm that enables accurate electromagnetic characterization of antennas interacting with complex spherical environments, with strong potential for future applications in biomedical systems, radome design, and reconfigurable electromagnetic structures.

#### APPENDIX A

##### VECTOR SPHERICAL WAVES AND SPECIAL FUNCTIONS

Vector spherical harmonics serve as essential building blocks for expanding vector fields in spherical coordinates. They are defined as follows [18, Appendix C.4]:

$$\begin{aligned} \mathbf{A}_{1\sigma ml}(\hat{\mathbf{r}}) &= \frac{1}{\sqrt{l(l+1)}} \nabla Y_{\sigma ml}(\hat{\mathbf{r}}) \times \mathbf{r} \\ \mathbf{A}_{2\sigma ml}(\hat{\mathbf{r}}) &= \frac{1}{\sqrt{l(l+1)}} r \nabla Y_{\sigma ml}(\hat{\mathbf{r}}) \\ \mathbf{A}_{3\sigma ml}(\hat{\mathbf{r}}) &= \hat{\mathbf{r}} Y_{\sigma ml}(\hat{\mathbf{r}}). \end{aligned} \quad (31)$$

Here,  $Y_{\sigma ml}(\hat{\mathbf{r}})$  denotes the scalar spherical harmonic, given by

$$Y_{\sigma lm}(\hat{\mathbf{r}}) = \sqrt{\frac{2 - \delta_{m0}}{2\pi}} \tilde{P}_l^m(\cos \theta) \begin{cases} \cos(m\varphi) \\ \sin(m\varphi) \end{cases} \quad (32)$$

where  $\tilde{P}_l^m(x)$  is the normalized associated Legendre function and  $\delta_{ij}$  is the Kronecker delta.

Using these harmonics, the vector spherical wave functions can be expressed compactly as:

$$\begin{aligned} \mathbf{u}_{1\sigma ml}^{(p)}(k\mathbf{r}) &= R_{1l}^{(p)}(kr) \mathbf{A}_{1\sigma ml}(\hat{\mathbf{r}}) \\ \mathbf{u}_{2\sigma ml}^{(p)}(k\mathbf{r}) &= R_{2l}^{(p)}(kr) \mathbf{A}_{2\sigma ml}(\hat{\mathbf{r}}) + R_{3l}^{(p)}(kr) \mathbf{A}_{3\sigma ml}(\hat{\mathbf{r}}). \end{aligned}$$

The scalar radial functions  $R_{\tau l}^{(p)}(kr)$  are constructed from Riccati-type special functions:

$$\begin{aligned} R_{1l}^{(p)}(kr) &= \frac{z_l^{(p)}(kr)}{kr} \\ R_{2l}^{(p)}(kr) &= \frac{[z_l^{(p)}(kr)]'}{kr} \\ R_{3l}^{(p)}(kr) &= \sqrt{l(l+1)} \frac{z_l^{(p)}(kr)}{(kr)^2} \end{aligned} \quad (33)$$

where  $z_l^{(1)}(x) \equiv \psi_l(x)$  and  $z_l^{(4)}(x) \equiv \xi_l(x)$  are the Riccati-Bessel and Riccati-Hankel functions, respectively. Their explicit definitions are:

$$\psi_l(x) = \sqrt{\frac{\pi x}{2}} J_{l+\frac{1}{2}}(x) \xi_l(x) = \sqrt{\frac{\pi x}{2}} H_{l+\frac{1}{2}}^{(2)}(x) \quad (34)$$

with  $J_n(x)$  and  $H_n^{(2)}(x)$  denoting the cylindrical Bessel and second-kind Hankel functions, respectively.

#### REFERENCES

- [1] J. Kim and Y. Rahmat-Samii, "Implanted antennas inside a human body: Simulations, designs, and characterizations," *IEEE Trans. Microw. Theory Tech.*, vol. 52, no. 8, pp. 1934–1943, Aug. 2004, doi: 10.1109/TMTT.2004.832018.
- [2] M. Gao, D. Nikolayev, Z. Sipus, and A. K. Skriverik, "Physical insights and design principles for efficient wireless implantable bioelectronics," *Cell Rep. Phys. Sci.*, p. 102627, Jun. 2025, doi: 10.1016/j.xcrp.2025.102627.
- [3] A. K. Skriverik, M. Bosiljevac, and Z. Sipus, "Fundamental limits for implanted antennas: Maximum power density reaching free space," *IEEE Trans. Antennas Propag.*, vol. 67, no. 8, pp. 4978–4988, Aug. 2019, doi: 10.1109/TAP.2019.2891697.
- [4] N. Ha-Van, S. A. Tretyakov, and C. R. Simovski, "Optimal frequencies for wireless power transfer through biological tissues," *IEEE Open J. Antennas Propag.*, 2025.
- [5] D. Nikolayev, A. K. Skriverik, J. S. Ho, M. Zhadobov, and R. Sauleau, "Reconfigurable dual-band capsule-conformal antenna array for in-body bioelectronics," *IEEE Trans. Antennas Propag.*, vol. 70, no. 5, pp. 3749–3761, May 2022, doi: 10.1109/TAP.2021.3138264.
- [6] I. V. Soares, M. Gao, Z. Sipus, A. K. Skriverik, J. S. Ho, and D. Nikolayev, "Wireless powering efficiency of deep-body implantable devices," *IEEE Trans. Microw. Theory Tech.*, vol. 71, no. 6, pp. 2680–2692, Jun. 2023, doi: 10.1109/TMTT.2022.3231492.
- [7] C.-T. Tai, *Dyadic Green Functions in Electromagnetic Theory*, 2nd ed., ser. IEEE Series on Electromagnetic Waves. Piscataway, NJ: IEEE Press, 1994.
- [8] L.-W. Li, P.-S. Kooi, M.-S. Leong, and T.-S. Yee, "Electromagnetic dyadic Green's function in spherically multilayered media," *IEEE Trans. Microw. Theory Tech.*, vol. 42, no. 12, pp. 2302–2310, Dec. 1994.
- [9] V. I. Okhmatovski and A. C. Cangellaris, "Efficient calculation of the electromagnetic dyadic Green's function in spherical layered media," *IEEE Trans. Antennas Propag.*, vol. 51, no. 12, pp. 3209–3220, Dec. 2003, doi: 10.1109/TAP.2003.820952.
- [10] S. K. Khomas, "Electromagnetic radiation by antennas of arbitrary shape in a layered spherical media," *IEEE Trans. Antennas Propag.*, vol. 57, no. 12, pp. 3827–3834, Dec. 2009, doi: 10.1109/TAP.2009.2033444.
- [11] T. Yu, C. Yin, and H. Liu, "Numerical analysis of single microstrip antenna and antennas array in spherically layered media," *IEEE Trans. Antennas Propag.*, vol. 63, no. 11, pp. 5180–5185, Nov. 2015, doi: 10.1109/TAP.2015.2478142.
- [12] C. G. Montgomery, R. H. Dicke, and E. M. Purcell, Eds., *Principles of Microwave Circuits*. Iet, 1987.
- [13] C. Della Giovampaola, E. Martini, A. Toccafondi, and S. Maci, "A hybrid PO/generalized-scattering-matrix approach for estimating the reflector induced mismatch," *IEEE Trans. Antennas Propag.*, vol. 60, no. 9, pp. 4316–4325, Sep. 2012, doi: 10.1109/TAP.2012.2207062.
- [14] J. E. Hansen, Ed., *Spherical Near-Field Antenna Measurements*. London, U.K.: Peter Peregrinus Ltd., 1988.



- [15] A. Greenleaf, Y. Kurylev, M. Lassas, and G. Uhlmann, "Invisibility and inverse problems," *Bull. Amer. Math. Soc.*, vol. 46, pp. 55–97, 2009.
- [16] *Generalized Scattering Matrix Framework for Modeling Implantable Antennas in Multilayered Spherical Media*. Accessed: Jul. 17, 2025. [Online] Available: <https://github.com/saintpredor/GSM-Framework-for-Implantable-Antennas>.
- [17] J. Song and W. C. Chew, "Error analysis for the truncation of multipole expansion of vector Green's functions [EM scattering]," *IEEE Microw. Wireless Compon. Lett.*, vol. 11, no. 7, pp. 311–313, Jul. 2001.
- [18] G. Kristensson, *Scattering of Electromagnetic Waves by Obstacles*, Edison, NJ, USA: SciTech Publishing, 2016.
- [19] W. C. Chew, *Waves and Fields in Inhomogeneous Media*, ser. IEEE Press Series on Electromagnetic Waves. Piscataway, NJ: IEEE Press, 1995.
- [20] V. Losenicky, L. Jelinek, M. Capek, and M. Gustafsson, "Method of moments and T-matrix hybrid," *IEEE Trans. Antennas Propag.*, vol. 70, no. 5, pp. 3560–3574, May 2022, doi: 10.1109/TAP.2021.3138265.
- [21] J. Liska, M. Gao, L. Jelinek, E. R. Algarp, A. K. Skrivervik, and M. Capek, "Maximum radiation efficiency of arbitrarily shaped implantable antennas," *IEEE Trans. Antennas Propag.*, vol. 72, no. 4, pp. 3507–3516, Apr. 2024, doi: 10.1109/TAP.2024.3365860.
- [22] P. C. Waterman, "Matrix formulation of electromagnetic scattering," *Proc. IEEE*, vol. 53, no. 8, pp. 805–812, Aug. 1965, doi: 10.1109/PROC.1965.4058.
- [23] J. Rubio, M. A. González, and J. Zapata, "Generalized-scattering-matrix analysis of a class of finite arrays of coupled antennas by using 3-D FEM and spherical mode expansion," *IEEE Trans. Antennas Propag.*, vol. 53, no. 3, pp. 1133–1144, 2005.
- [24] C. Shi, J. Pan, X. Gu, S. Liang, and L. Zuo, "Generalized scattering matrix of antenna: Moment solution, compression storage and application," *IEEE Trans. Antennas Propag.*, 2025.
- [25] S. Rao, D. Wilton, and A. Glisson, "Electromagnetic scattering by surfaces of arbitrary shape," *IEEE Trans. Antennas Propag.*, vol. 30, no. 3, pp. 409–418, May 1982, doi: 10.1109/TAP.1982.1142818.
- [26] C.-W. Qiu, S. Zouhdi, and A. Razek, "Modified spherical wave functions with anisotropy ratio: Application to the analysis of scattering by multilayered anisotropic shells," *IEEE Trans. Antennas Propag.*, vol. 55, no. 12, pp. 3515–3523, Dec. 2007, doi: 10.1109/TAP.2007.910491.
- [27] C. Shi, S. Liang, J. Pan, X. Gu, and L. Zuo, "Generalized scattering matrix synthesis for hybrid systems with multiple scatterers and antennas using independent structure simulations," *arXiv preprint arXiv:2503.17616*, 2025.